Title

Monte Carlo modeling of low-energy electron-induced secondary electron emission yields in micro-architected boron nitride surfaces

Authors

Chang, Hsing-Yin
Alvarado, Andrew
Weber, Trey
et al.

Publication Date

2019-09-01

DOI

10.1016/j.nimb.2019.05.079

Peer reviewed

Applied Surface Science 450 (2018) 190–199

Contents lists available at ScienceDirect

Applied Surface Science

journal homepage: www.elsevier.com/locate/apsusc

Full Length Article

Calculation of secondary electron emission yields from low-energy electron deposition in tungsten surfaces

Hsing-Yin Chang [a,*], Andrew Alvarado [a], Jaime Marian [a,b]

[a] Department of Materials Science and Engineering, University of California, Los Angeles, CA 90095, USA
[b] Department of Mechanical and Aerospace Engineering, University of California, Los Angeles, CA 90095, USA

ARTICLE INFO

Article history:
Received 29 November 2017
Revised 1 February 2018
Accepted 16 April 2018
Available online 22 April 2018

Keywords:
Monte Carlo simulation
Electron-matter interactions
Secondary electron emission
Symbolic regression

ABSTRACT

We present calculations of secondary electron emission (SEE) yields in tungsten as a function of primary electron energies between 100 eV and 1 keV and incidence angles between 0 and 90°. We conduct a review of the established Monte Carlo methods to simulate multiple electron scattering in solids and select the best suited to study SEE in high-Z metals. We generate secondary electron yield and emission energy functions of the incident energy and angle and fit them to bivariate fitting functions using symbolic regression. We compare the numerical results with experimental data, with good agreement found. Our calculations are the first step towards studying SEE in nanoarchitected surfaces for electric propulsion chamber walls.

1. Introduction

Secondary electron emission (SEE) is the emission of free electrons from a solid surface, which occurs when these surfaces are irradiated with external (also known as *primary*) electrons. SEE is an important process in surface physics with applications in numerous fields, such as electric propulsion [1–5], particle accelerators [6], plasma-walls in fusion reactors [7–11], electron microscopy and spectroscopy [12,13], radio frequency devices [14–16], etc. In Hall thrusters for electric propulsion, a key component is the channel wall lining protecting the magnetic circuits from the discharge plasma. These channel walls are a significant factor in Hall thruster performance and lifetime through its interactions with the discharge plasma. These interactions are governed by the sheath formed along the walls, and so the properties of the sheath determine the amount of electron energy absorbed by the wall, which in turn affects the electron dynamics within the bulk discharge [1,17–19]. Furthermore, the energy imparted by the sheath to the ions within the discharge determines the impact energy and incident angle of ions upon the surface, thus affecting the amount of material sputtered and consequently the wall erosion rate [20,21]. Thus, understanding how SEE affects sheath stability is crucial to make predictions of channel wall lifetime.

Recently, a new wall concept based nano-architected surfaces has been proposed to mitigate surface erosion and SEE [22–25]. Demonstration designs based on high-Z refractory materials have been developed, including architectures based on metal nanowires and nanofoams [26–30]. The idea behind these designs is to take advantage of very-high surface-to-volume ratios to reduce SEE and ion erosion by internal trapping and redeposition. Preliminary designs are based on W, W/Mo, and W/Re structures, known to have intrinsically low sputtering yields secondary electron emission propensity. A principal signature of electron discharges in plasma thrusters is the low primary electron energies expected in the outer sheath, on the order of 100 eV, and only occasionally in the several hundred eV regime. Accurate experimental measurements are exceedingly difficult in this energy range due to the limited thickness of the sheath layer, which is often outside the resolution of experimental probes [31–33]. Modeling then suggests itself as a complementary tool to experiments to increase our qualitative and quantitative understanding of SEE processes.

To quantify the net SEE yield from these surfaces, models must account for the explicit geometry of these structures, which requires high spatial resolution and the capacity to handle large numbers of degrees of freedom. However a precursor step to the development of these descriptions is the characterization of the SEE yield functions as a function of incident electron energy and angle of incidence in flat surfaces. Once defined, these functions can then be implemented at the level of each surface element to create a spatially-dependent emission picture of the SEE process. This is the subject of the present paper: to calculate SEE yield functions from flat W surfaces in terms of primary electron energy and incidence angle. To this end, we carry out Monte Carlo calculations

* Corresponding author.
E-mail address: irischang@ucla.edu (H.-Y. Chang).

https://doi.org/10.1016/j.apsusc.2018.04.155
0169-4332/

of electron scattering processes in pure W using a series of scattering models specifically tailored to high-Z metals.

The paper is organized as follows. First we discuss the theoretical models employed to study electron scattering in W. This is followed by a discussion of the implementation of these models under the umbrella of a Monte Carlo framework. Our results follow, with emphasis on emission yield and energy functions. We finalize with the conclusions and the acknowledgments.

2. Theory and methods

2.1. Electron scattering theory

The present model assumes that electrons travel in an isotropic homogeneous medium undergoing collisions with bulk electrons. Each collision results in a trajectory change with an associated energy loss, which depend on the nature of the electron-electron interaction. As well, collisions may result in secondary electron production. We classify interactions into two broad categories: elastic and inelastic, each characterized by the corresponding collision mean free path and an angular scattering function. These processes are then simulated using a Monte Carlo approach, where collisions are treated stochastically and trajectories are tracked as a sequence of scattering events until the resulting secondary electrons are either thermalized or emitted back from the surface.

Scattering theory provides formulas for the total and the differential scattering cross sections, from which the mean free path and polar scattering angle can be obtained, respectively. Next, we provide a brief description of the essential theory behind each of the distinct collision processes considered here. Our implementation accounts for the particularities of low-energy electron scattering in high-Z materials. The validity range of the present approach in Z, which is for atomic numbers up to 92, and in primary electron energy, from 100 eV to 30 keV.

2.2. Elastic scattering

Elastic scattering takes place between electrons and atomic nuclei, which–due to the large mass difference–results in no net energy loss for the electron, only directional changes [34]. A widely used electron-atom elastic scattering cross section is the screened Rutherford scattering cross section [35,36], which provides a simple analytical form and is straightforward to implement into a Monte Carlo calculation. However, the screened Rutherford scattering is generally not suitable for low-energy electron irradiation of high-Z metals.

In this work, we use an empirical total elastic scattering cross section proposed by Browning et al. (1994), which is obtained via fitting to trends in tabulated Mott scattering cross section data set described by Czyżewski *et al.* [37] using the relativistic Hartree-Fock potential. This is amenable to fast Monte Carlo computations at a high degree of accuracy. The equation for the total elastic scattering cross section is [38,39]:

$$\sigma_{el} = \frac{3.0\times10^{-18}Z^{1.7}}{(E + 0.005Z^{1.7}E^{0.5} + 0.0007Z^2/E^{0.5})} \quad [\mathrm{cm}^2], \tag{1}$$

which is valid for atomic numbers up to 92 and for energies from 100 eV to 30 keV. From this, the elastic mean free path can be derived:

$$\lambda_{el} = \frac{1}{N\sigma_{el}} = \frac{AW}{N_a\rho\sigma_{el}} \quad [\mathrm{cm}] \tag{2}$$

where N is the number of atoms per cm^3. For its part, the polar scattering angle can be obtained by a random number R uniformly distributed between 0 and 1:

$$R = \frac{\int_0^{\theta}\left(\frac{d\sigma_R}{d\Omega}\right)d\Omega}{\int_0^{\pi}\left(\frac{d\sigma_R}{d\Omega}\right)d\Omega} \tag{3}$$

where $d\Omega = 2\pi\sin\theta d\theta$ is the infinitesimal solid angle.

Solving the above equation for the Mott cross section requires numerical integration, as there is no simple analytical form for the polar scattering angle θ. Drouin [40] et al. (1994) gives a parameterized form of the function as

$$\cos\left(\theta_i^{\beta}\right) = 1 - \frac{2\alpha R^*}{1+\alpha-R^*} \tag{4}$$

where θ_i is given in degrees. Then first parameter, α, as a function of the energy is obtained with

$$\log_{10}(\alpha) = a + b\log_{10}(E) + c\log_{10}^2(E) + \frac{d}{e^{\log_{10}(E)}} \tag{5}$$

where E is the energy in keV, a, b, c and d are constants that have been calculated using the least-square method, and $e = 2.7813$. A tabulation form of a, b, c and d for the first 94 elements of the periodic table is found in Table 2 in Ref. [40]. For tungsten ($Z = 74$), $a = -2.0205, b = -1.2589, c = 0.271737, d = -0.695477$.

The second parameter, β, is calculated using the following equations:

$$\begin{aligned} \beta^* &= a + b\sqrt{E}\ln(E) + \frac{c\ln(E)}{E} + \frac{d}{E} \\ \beta &= \begin{cases} 1 & \text{if} \quad \beta^* > 1 \\ \beta^* & \text{if} \quad \beta^* \le 1 \end{cases} \end{aligned} \tag{6}$$

where E is the energy in keV, a, b, c and d are constants that have been obtained using the least-squares fitting. A tabulation form of a, b, c and d for the first 94 elements of the periodic table is found in Table 3 in reference [40]. For tungsten ($Z = 74$), $a = 0.71392, b = 0.00197916, c = -0.0172852, d = -0.0570799$.

The third parameter, R^* is obtained as:

$$R^* = R \times R_{max} \tag{7}$$

where R is a random number uniformly distributed between 0 and 1 and R_{max} is the value of R^* obtained when θ_i is set to 180° in Eq. (4), i.e.:

$$R_{max} = \frac{\cos(180^{\beta}) + \alpha\cos(180^{\beta}) - 1 - \alpha}{\cos(180^{\beta}) - 1 - 2\alpha} \tag{8}$$

The azimuthal angle ϕ can take any value in the range 0–2π as determined by a random number R uniformly distributed in that range.

$$\phi = 2\pi R \tag{9}$$

2.3. Inelastic scattering

In contrast to elastic scattering, inelastic scattering implies collisional energy loss. There are several distinct inelastic interaction processes to be considered, including phonon excitation, secondary electron excitation, *Bremsstrahlung* or continuum X-ray generation, and ionization of inner electron shells. Each mechanism is described by a model that provides expressions for the scattering cross section, scattering angle, and mean free path. The physics behind some of these processes is complex, and detailed expressions for the associated cross sections are often unavailable [41,42].

In conventional Monte Carlo approaches, Bethe's theory of stopping power based on a continuous slowing-down approximation (CSDA) [35,43,44] is used to describe the average energy dissipation rate of a penetrating electron along its path, in which the contribution of all possible excitation processes to the energy loss has been represented by a factor called the mean ionization

energy, J. However, this formula is not valid in the low energy regime (0.1–30 keV) or for high atomic number elements ($Z >$ 30). To resolve this, much effort has been devoted to modifying the Bethe formula, from which systematization of tabulated electron stopping powers for various elements and attempts to simplify the calculations have emerged. [45–49] In general, the use of these formulas for elements or compounds with fitting parameters requires a detailed and accurate supply of experimental data on which to base its physics and against which to test its predictions. [50] Nevertheless, the CSDA strategy may still become obsolete when an electron occasionally loses a large fraction of its energy in a single collision as well as when secondary electron emission distribution spectra are required. To develop a more comprehensive Monte Carlo approach, incorporating differential cross sections for each of the inelastic events seems necessary [51–54].

Ritchie et al. (1969) have demonstrated that the stopping power described by Bethe's formula is obtained by the summation of theoretical stopping powers for conduction electron, plasmon and L-shell electron excitations for aluminum. [53] Fitting (1974) [55] has also shown that this stopping power derived by Ritchie *et al.* is in very good agreement with experimental investigation even in the energy range between 0.8 and 4 keV. Accordingly, the model of inelastic scatterings considered in the present approach are electron-conduction electron scattering, electron-plasmon scattering and electron-shell electron scattering as shown in Fig. 1.

2.3.1. Inner shell electron ionization

The classical formalism of Gryziński (1965) [56–59] has been adopted to describe inner-shell electron ionization. The differential cross section can be written as:

$$\frac{d\sigma_s(\Delta E)}{d\Delta E} = \frac{\pi e^4}{(\Delta E)^3}\frac{E_B}{E}\left(\frac{E}{E+E_B}\right)^{3/2}\left(1-\frac{\Delta E}{E}\right)^{E_B/(E_B+\Delta E)} \times\left\{\frac{\Delta E}{E_B}\left(1-\frac{E_B}{E}\right)+\frac{4}{3}\ln\left[2.7+\left(\frac{E-\Delta E}{E_B}\right)^{1/2}\right]\right\} \quad (10)$$

where $\Delta E, E$ and E_B are the energy loss, the primary electron energy, and the mean electron binding energy, respectively.

At each inelastic scattering event, the energy loss of the primary electron resulting from an inelastic scattering with the shell is determined using a uniform random number R and by finding a value of ΔE which satisfies the relation

$$R = \int_{E_B}^{\Delta E}\frac{d\sigma_s(\Delta E')}{d\Delta E'}\frac{d\Delta E'}{\sigma_s} \quad (11)$$

The integral is given by the approximate expression [60]

$$\int_{E_B}^{\Delta E}\frac{d\sigma_s(\Delta E')}{d\Delta E'}d\Delta E' = \left(\frac{\pi n_s e^4}{EE_B}\right)\left(\frac{E}{E+E_B}\right)^{3/2}\left(1-\frac{\Delta E}{E}\right)^{1+(E_B/(E_B+\Delta E))} \times\left\{\frac{\Delta E}{E_B}+\frac{2}{3}\left(1-\frac{\Delta E}{E}\right)\ln\left[2.7+\left(\frac{E-\Delta E}{E_B}\right)^{1/2}\right]\right\} \times\frac{E_B^2}{\Delta E^2} \quad (\Delta E \geqslant E_B) \quad (12)$$

where n_s is the occupation number of electrons in the shell.

The total cross section of the inner electron excitation is obtained by integrating over all possible values of ΔE

$$\sigma_s(E) = \int_{E_B}^{\Delta E_{max}}\frac{d\sigma_s(\Delta E')}{d\Delta E'}d\Delta E' = 6.5141\times10^{-14}\frac{n_s}{E_B^2}\frac{E_B}{E}\left(\frac{E-E_B}{E+E_B}\right)^{3/2} \times\left[1+\frac{2}{3}\left(1-\frac{E_B}{2E}\right)\ln\left(2.7+\left(\frac{E}{E_B}-1\right)^{1/2}\right)\right][\mathrm{cm}^2] \quad (13)$$

where the maximum amount of energy that can be lost ΔE_{max} is equal to E.

When the random number selection gives an energy loss less than the binding energy E_B, the actual energy loss is set to be zero. The scattering angle for an inelastic electron-electron event is calculated according to the binary collision approximation (BCA) as

$$\sin\theta = \left(\frac{\Delta E}{E}\right)^{1/2} \quad (14)$$

In tungsten, for primary energies $E \leqslant 1$ keV, inner shell electron ionization can be safely neglected, as the energy is insufficient to knock out inner shell electrons.

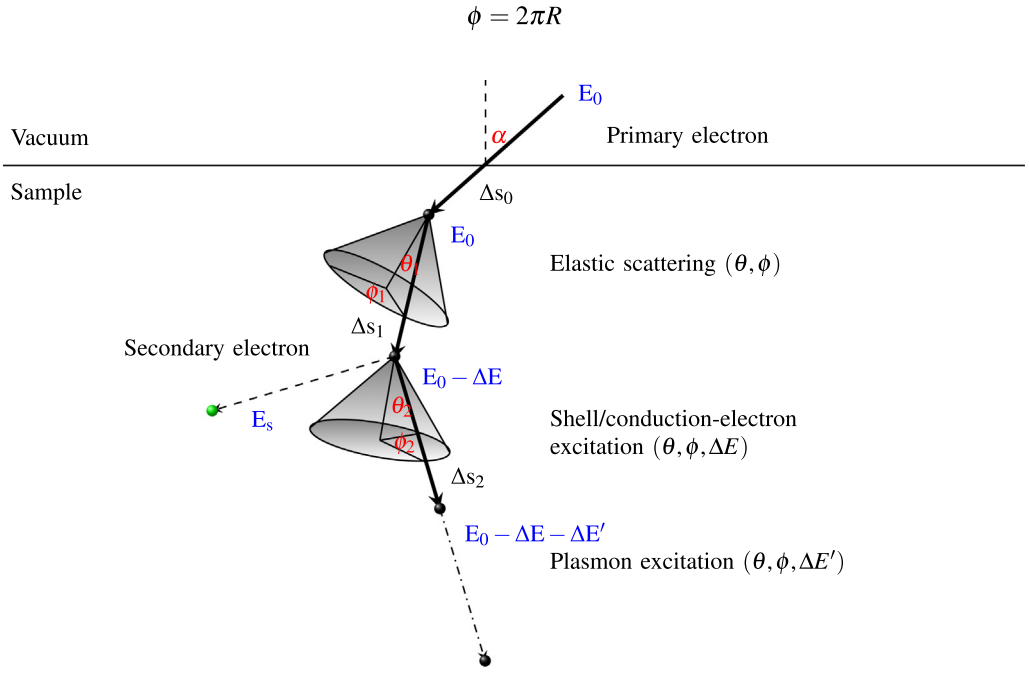

Fig. 1. Schematic diagram of the discrete collision model of electron scattering simulated using Monte Carlo calculation.

2.3.2. Conduction electron excitation

For metals bombarded by electrons, Streitwolf (1959) [61] has given the differential cross section for conduction electron excitation by using perturbation theory as

$$\frac{d\sigma_c(E_{SE})}{dE_{SE}} = \frac{e^4 N_a \pi}{E(E_{SE} - E_F)^2} \tag{15}$$

The total energy loss cross section $\sigma_c(E)$ can be obtained by integrating the above expression between the lower energy limit $E_F + \Phi$ and the upper energy limit E:

$$\sigma_c(E_{SE}) = \frac{e^4 N_a \pi}{E} \frac{E - E_F - \Phi}{\Phi(E - E_F)} \tag{16}$$

The obtained relation samples the energy of the secondary electron with the random number R:

$$E_{SE}(R) = [RE_F - A(E_F + \Phi)]/(R - A) \tag{17}$$

where Φ is the workfunction and $A = (E - E_F)/(E - E_F - \Phi)$. Once the energy of the secondary electron is known (equal to the energy lost by the primary electron), the next question is how the two electrons are oriented in space. More accurate results can be obtained if the classical BCA is used, which results from conservation of energy and momentum. The azimuthal angle is again assumed to be isotropic. For the incident electron, we then have:

$$\sin\theta = \sqrt{\frac{\Delta E}{E}} \tag{18}$$

$$\phi = 2\pi R$$

where ΔE is the energy lost by the incident electron. For the secondary electrons, scattering angles can be calculated as follow:

$$\sin\vartheta = \cos\theta \tag{19}$$

$$\varphi = \pi + \phi \tag{20}$$

The above expression is applied to the inner shell electron as well as conduction electron excitations.

2.3.3. Plasmon excitation

The Coulomb field of the primary electron can perturb electrons of the solid at relatively long range as it passes through the target. The primary electron can excite oscillations (known as *plasmons*) in the conduction electron gas that exists in a metallic sample with loosely bound outer shell electrons. The differential cross section for plasmon excitation is given by Ferrel (1956) [62–64], per conduction-band electron per unit volume

$$\frac{d\sigma_p(E,\theta)}{d\Omega} = \frac{1}{2\pi a_0} \frac{\theta_p}{\theta^2 + \theta_p^2} \tag{21}$$

$$\theta_p = \frac{\Delta E}{2E} = \frac{\hbar\omega_p}{2E} \tag{22}$$

where a_0 is Bohr radius (5.29×10^{-9} [cm]). In plasmon scattering, primary electron energy loss is quantized and ranges from 3 to 30 eV depending on the target species, which is detected as strong features in electron energy-loss spectra (EELS). Plasmon scattering is so sharply peaked forward that the total plasmon cross section, σ_p, can be found by setting $d\Omega = 2\pi\sin\theta d\theta \approx 2\pi\theta d\theta$:

$$\sigma_p = \int d\sigma_p(\theta) = \frac{\theta_p}{2\pi a_0} \int_0^{\theta_1} \frac{2\pi\theta d\theta}{\theta^2 + \theta_p^2} \tag{23}$$

By assuming the upper integration limit as $\theta_1 = 0.175$ rad, where $\theta \approx \sin\theta$, and incorporating the factor $(n_c AW/N_a\rho)$ to put the cross section on a per-atom/cm^2 basis gives the total cross section of the plasmon excitation as

$$\sigma_p = \frac{n_c AW\theta_p}{2N_a\rho a_0}\left[\ln(\theta_p^2 + 0.175^2) - \ln(\theta_p^2)\right] \quad [\text{cm}^2] \tag{24}$$

where n_c is the number of conduction-band electrons per atom. Essentially, the scattering of primary electrons due to plasmon excitations is restricted with $\theta < \theta_{max}$, k_c being the cut-off wavenumber. Since θ_{max} is so small, about 10 mrad in the energy range discussed here, the angular deflection due to plasmon excitation is neglected in this approach.

Again, the azimuthal angle ϕ can take on any value in the range 0 to 2π selected by a random number R uniformly distributed in that range.

$$\phi = 2\pi R$$

3. Monte Carlo calculations

As indicated above, electron trajectories are simulated by generating a spatial sequence of collisions by randomly sampling from among all possible scattering events. The distance traveled by electrons in between collisions, Δs, is assumed to follow a Poisson distribution defined by the total mean free path λ_T [35]

$$\Delta s = -\lambda_T \log\ R \tag{25}$$

where

$$\frac{1}{\lambda_T} = \frac{1}{\lambda_{el}} + \frac{1}{\lambda_p} + \frac{1}{\lambda_c} + \frac{1}{\lambda_s} = N(\sigma_{el} + \sigma_p + \sigma_c + \sigma_s), \tag{26}$$

N is the number of atoms per cm^3 and R is a random number uniformly distributed in the interval $(0, 1]$. From this, we define the following probabilities:

$P_{el} = \lambda_T/\lambda_{el}$: the probability that the next collision will be elastic
$P_p = \lambda_T/\lambda_p$: the probability that the next collision will cause a plasmon excitation
$P_c = \lambda_T/\lambda_c$: the probability that the next collision will cause a conduction electron excitation$P_s = \lambda_T/\lambda_s$: the probability that the next collision will cause an inner shell electron excitation (27)

The type of collision is then chosen based on the following partition of the value of R:

$0 < R \leqslant P_{el} \Rightarrow$ elastic scattering
$P_{el} < R \leqslant P_{el} + P_p \Rightarrow$ plasmon excitation
$P_{el} + P_p < R \leqslant P_{el} + P_p + P_c \Rightarrow$ conduction electron excitation
$P_{el} + P_p + P_c < R \leqslant 1 (\equiv P_{el} + P_p + P_c + P_s) \Rightarrow$ inner shell electron excitation (28)

The flow diagram corresponding to the implementation of the model just described is provided in Appendix C. Following this approach, electron trajectories[1] are tracked in the energy-position space until a scattered electron either thermalizes, i.e. its energy follows below the surface escape threshold (Fermi level plus workfunction) within the material, or reaches the surface with a velocity having a component pointing along the surface normal with an energy larger than the escape threshold. In the latter case, the electron is tallied as a secondary electron and its energy and exit angle

[1] Trajectories are generated by stitching together each sequence of discrete collision events and referring each collision point to a global *laboratory* frame of reference. The coordinate transformation employed here can be found in Ref. [65] and is provided in Appendix D.

are recorded.

Next we analyze the Monte Carlo calculations performed following this method and present results of secondary electron yield and emission energies as a function of primary electron energy and angle of incidence.

4. Results

The total secondary electron yield for perfectly-flat tungsten surfaces is calculated for primary incident angles of 0°, 30°, 45°, 60°, 75° and 89° measured off the surface normal, and incident energies in the range 100–1000 eV. In this work, the typical number of primary particles simulated ranges between 10^4 and 10^5, which generally results in statistical errors around 3%. Our first set of results includes the energy and angular distributions of emitted secondary electrons for normal incidence and 100 eV and a primary electron energy of 100 eV. The normalized distributions are given in Fig. 2a and b, where the characteristic energy decay of $1/E$ and cosine angular distribution of collisional processes can be appreciated in each case. One of the advantages of using a discrete event method for simulating electron scattering processes is that useful information of discrete nature can be extracted from the data. For example, in Fig. 3a we show the depths from which secondary electrons are emitted (last scattering collision inside the material) as well as the depth distribution of thermalized (non-emitted) electrons, i.e. the depth at which electrons attain an energy less than the threshold. Both cases are for normal incidence and $E = 100$ eV. In Fig. 3b we break the total number of collisions down into the main scattering

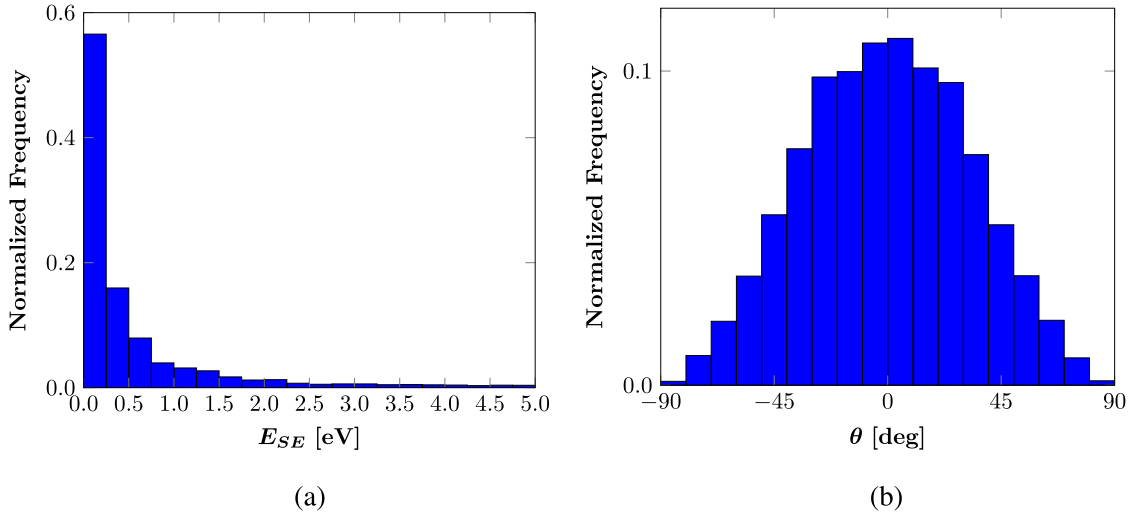

Fig. 2. Normalized distributions for 100-eV primary electrons incident at 0°: (a) Energy distribution of secondary electrons; (b) Angular distribution of secondary electrons.

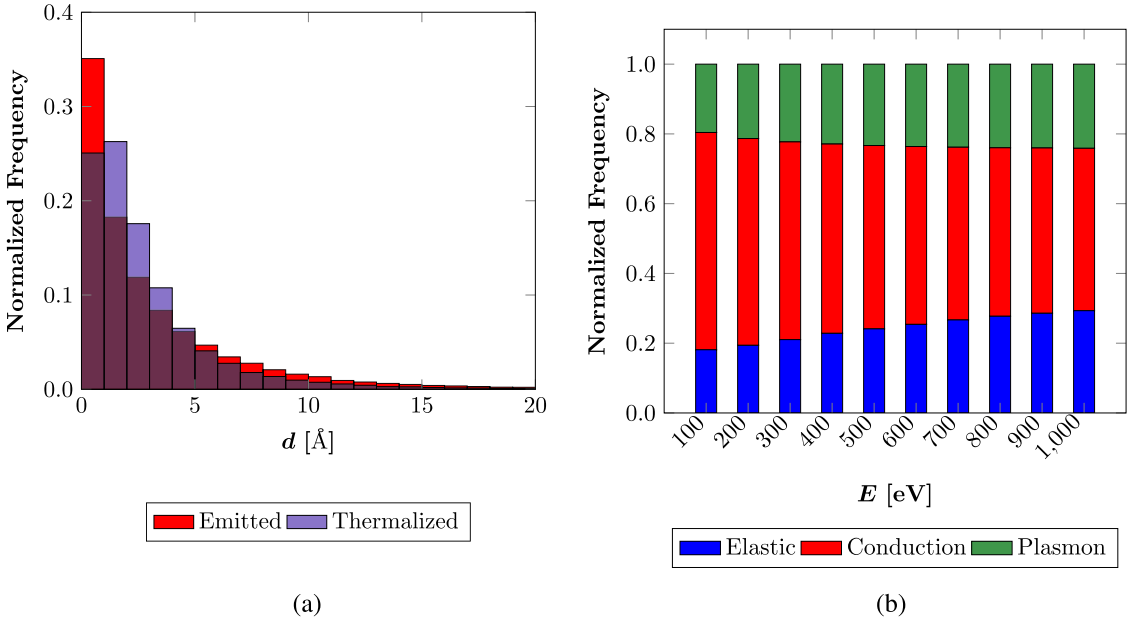

Fig. 3. (a) Depth distribution of both emitted and thermalized (captured) electrons for a primary electron energy and incident angle of 100 eV and 0°. (b) Relative occurrence of the main scattering mechanisms as a function of primary energy for normal incidence.

modes as a function of primary energy and normal incidence. It can be seen that scattering with conduction electrons is always the dominant mechanism, although its relative importance reduces with E.

Next, we plot the SEE yields as a function of primary electron energy for angles of incidence of 0 and 45° to facilitate comparison with existing experimental data and other published Monte Carlo simulation results. The results are shown in Fig. 4a and b, respectively, with error bars provided in each case. In general, the simulation results are found to agree reasonably well with experimental data. The agreement is slightly worse for 45° than for 0° incidence, which we rationalize in terms of the higher incidence direction. It is well-known that the fraction of reflected particles increases with the angle of incidence [71]. In addition, the roughness of 'real' experimental surfaces compared to the ideally-smooth ones in the model likely plays a significant role in the comparison. SEE yields as a function of E for all angles of incidence considered here are given in Fig. 5.

Surface plots of both SEE energy distributions and the yields are given in Fig. 6a and b As mentioned earlier, these data will be used in *ray-tracing* Monte Carlo simulations of SEE in arbitrary surface geometries. In these simulations, primary rays are generated above the material surface with the corresponding incident energy E. Intersections of these primary rays with surface elements determines the corresponding angle of incidence α. E and α are then used to sample from the data shown in, e.g., Fig. 2, after which secondary rays with appropriate energies E_{SE} and exit angles (sampled from a cosine distribution) are generated. These 'daughter' rays are themselves tracked in their interactions with other surface elements, after which the sequence is repeated and subsequent generations of rays are produced. This process goes on until rays either escape the surface with an upward velocity –in which case the event is tallied as a successful SEE event– or until their energy is below the threshold escape energy (Fermi level plus workfunction). However, directly interpolating from our data tables potentially hundreds of thousands of times can slow down the simulations considerably. To avoid that, it is more efficient to fit

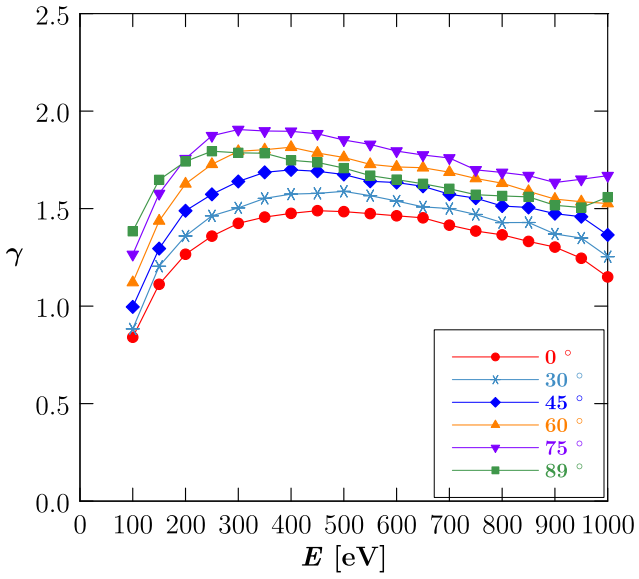

Fig. 5. Total SEE yield from an ideally-flat W as a function of primary electron energy, for electrons incident at 0°, 30°, 45°, 60°, 75° and 89°.

the data to suitable analytical expressions that can be evaluated very fast on demand. To this end, we fit our raw data to bivariate mathematical functions obtained using *symbolic regression* (SR), which is a type of genetic evolutionary algorithm for machine learning which utilizes evolutionary searches to determine both the parameters and the form of the fitting expressions simultaneously, to speed up our calculation. We have used the trial version of `Eureqa` [72,73], a commercial SR engine, to generate a catalog of potential candidate expressions for mathematical fitting. We then select the final expression by capping the fitting errors to be no higher than the intrinsic statistical errors of the Monte Carlo

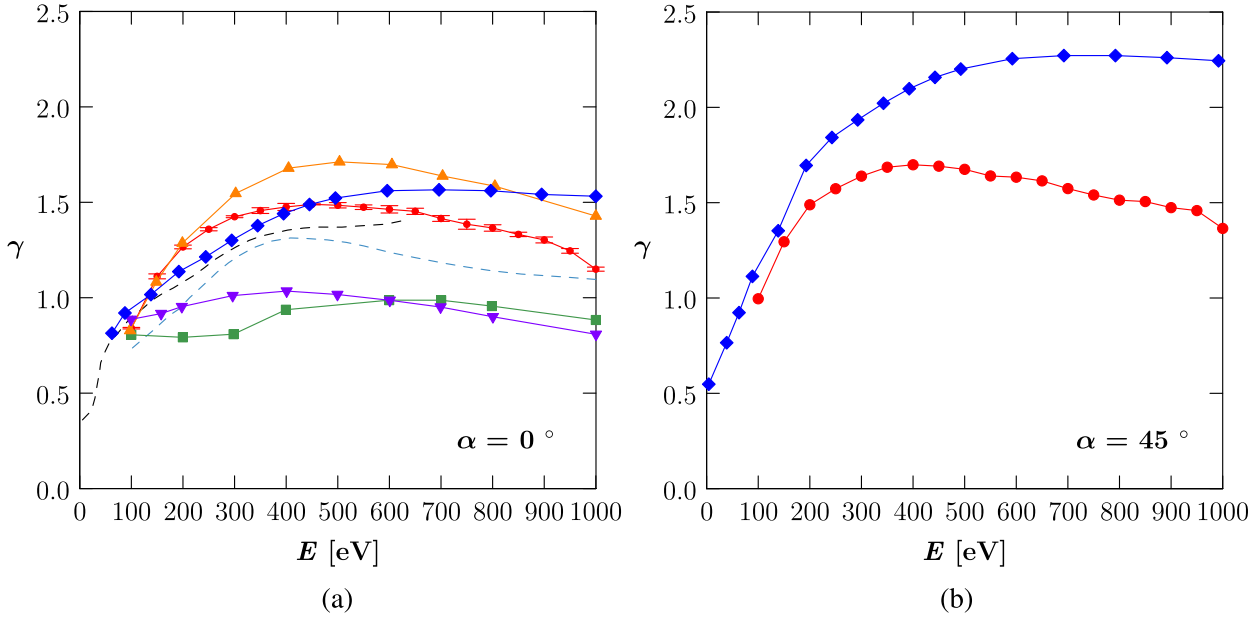

Fig. 4. (a) Total SEE yield from an ideally-flat W surface as a function of primary electron energy for electrons incident at 0°. • = this work; black dashed line = Ahearn (1931) [66]; cyan dashed line = Coomes (1939) [67]; ■ = Bronshtein and Fraiman (1969) [68]; ▲ = Ding et al. (2001) using the method where the SE is assumed to come from a distribution of electron energies in the valence band; ▼ = Ding *et al.* (2001) using the method where the SEs are assumed to originate from the Fermi level [69,70]; ◆ = Patino et al. (2016) [30]. (b) Total SEE yield from smooth W as a function of primary electron energy, for electrons incident at 45°. •=this work; ◆ = Patino et al. (2016) [30].

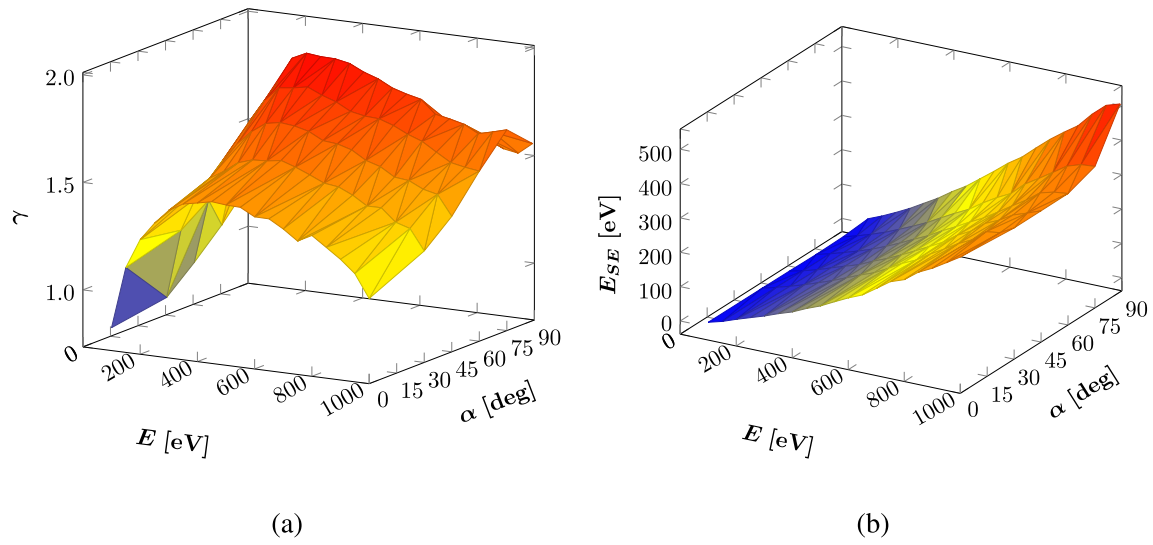

Fig. 6. (a) Surface plot of the total SEE yield from an ideally-flat W as a function of primary electron energy and angle of incidence. (b) Surface plot of the SEE energy distributions from an ideally-flat W as a function of primary electron energy and angle of incidence.

calculations ($\approx 3\%$). This ensures that the fitted functions always provide solutions to within the natural variability of the fitted data. Beyond that, we generally try to use functions that are well behaved numerically in as wide an energy range as possible, e.g. discarding those with logarithmic terms, etc. The final expressions for the total SEE yield and energy distributions are

$$\gamma(E,\alpha) = 3.05288 + 1.7949\times10^{-5}\alpha^2 + 6.15912\times10^{-7}E^2 + (3.71317\times10^{2} - \exp(4.8259\times10^{-2}\alpha))/(-8.760195\times10^{-1} - E) - 1.974\times10^{-4}E - 1.0971\times10^{-1}\cos(1.20187\times10^{-1} + 2.469421\alpha) \quad (29)$$

$$E_{SE}(E,\alpha) = 1.95\times10^{-1}E + 1.69\times10^{-4}E^2 + 1.48\times10^{-1}\alpha\sin(E) + 3.44\times10^{-15}E\alpha^7 - 6.54 \quad (30)$$

We note that these expressions do not necessarily reflect the physics behind SEE and are just intended for efficient numerical evaluations strictly in the ranges shown in the figures.

5. Discussion and conclusions

Electron-matter interactions are complex processes. To make the theoretical treatment of electron scattering a tractable analytical problem, it is assumed that elastic scattering occurs through the interatomic potential, while inelastic scattering only through electron–electron interactions. Evidently, the accuracy of the Monte Carlo simulations depends directly on how precisely the approximations introduced in the model are described. Most models treat elastic interactions within Mott's formalism [34] (or adaptations thereof). For their part, inelastic scattering processes in this work are considered individually, each one characterized by its own differential cross sections, corresponding to valence, inner shell, conduction, and plasmon electron excitation. In contrast, Ding et al. [69] use Penn's dielectric function [74] for electron inelastic scattering obtained from a modification of the statistical approximation. Many other models for metals account for valence interactions only [35,75,76]. Here, we improve in these models, although we do not capture the generation of SE from plasmon decay, backscattered electrons, reflected electrons, and transmitted electrons (coming out from the back side of the sample). This must be kept in mind when comparing the simulation results with experimental data (cf. Fig. 4). In this sense, it can be said that our results provide a first-order check of the importance of internal scattering processes, which helps us understand the governing physics behind SEE.

In any case, discrete event simulations–e.g. as the Monte Carlo model implemented in this paper–present the advantage that they provide a measure of the statistical errors associated with a given formulation. This is not just a numerical matter because experimental measurements themselves correspond to averages of a given realization of the scattering process. In the discrete approach the energy loss of electrons traveling through a solid is determined by considering different inelastic scattering processes–including conduction electron excitation, plasmon decay, and inner shell electron ionization–are considered individually, whereas within the so-called continuous slowing down approximation (CSDA), the overall inelastic scattering mechanisms are averaged out by using the total stopping power. From this point of view, the CSDA and the discrete-event simulation method would formally converge in the limit of an infinite number of events. Discrete simulations also allow a better physical and spatial dissection of electron scattering processes, providing spatial distributions and breakdowns among the different scattering mechanisms. This information is important to ascertain what scattering events dominate the secondary electron emission process in each material. This is what is shown in Fig. 3b, where the partition of scattering mechanisms for normal incidence and 100 eV primary energy is given. A disadvantage of discrete vs continuous simulations is, however, the longer computational cost required to obtain acceptable statistics. Modelers, therefore, must weigh in each of these factors (better spatial resolution and statistical information vs worse computational efficiency) and decide what approach to use.

To summarize, in this work we have carried out Monte Carlo calculations of low energy electron induced SE emission from flat tungsten surfaces. Our model includes multiple elastic and inelastic scattering processes, implemented via a discrete energy loss approach. We compare predictions of our model with other Monte Carlo techniques as well as experimental data, with generally good agreement found. We have calculated the total SEE yield and

secondary electron energy spectrum for primary electron beams at incident angles of 0°, 30°, 45°, 60°, 75° and 89°, in the range 100–1000 eV. We have used SR to obtain analytical expressions that represent the numerical data. These functions are currently being used in ray-tracing Monte Carlo simulations of SEE in arbitrary surface geometries.

Acknowledgement

The authors acknowledge support from the Air Force Office of Scientific Research (AFOSR), through award number FA9550-11-1-0282 with UCLA.

Appendix A. List of Symbols

a_0	Bohr radius
AW	atomic weight
Z	atomic number
N_a	Avogadro's number
ρ	density of the target
$N = \rho N_a/AW$	atomic number density
n_s	number of electrons in shell or subshell
n_c	number of conduction-band electrons per atom
e	electron charge
ϵ	permittivity of vacuum
m_e	mass of electron
$\hbar$	reduced Planck constant
ω_p	plasma frequency
E	primary electron energy
E_{SE}	secondary electron energy
E_F	Fermi energy
k_F	Fermi wave number
E_B	binding energy of the shell
$E_{pl} = \hbar\omega_p$	plasmon energy
ΔE	energy loss of primary electron
Φ	work function
J	mean ionization potential
α	incident angle of primary electron
σ_{el}	elastic scattering cross section
σ_p	plasmon excitation cross section
σ_c	conduction electron ionization cross section
σ_s	inner shell electron ionization cross section of
$d\sigma/d\Omega$	differential scattering cross section with respect to direction
$d\sigma/dE$	differential scattering cross section with respect to energy
λ_{el}	elastic mean free path
λ_p	plasmon excitation mean free path
λ_c	conduction electron excitation mean free path
λ_s	inner shell electron excitation mean free path
λ_T	total mean free path
θ	polar scattering angle of the primary electron
ϑ	polar scattering angle of the secondary electron
ϕ	azimuthal scattering angle of the primary electron
φ	azimuthal scattering angle of the secondary electron
θ_p	plasmon loss scattering angle
d	depth

Appendix B. Constants & kinematical quantities

$N_a = 6.022 \times 10^{23}$, Avogadro's number

$\epsilon = 8.85 \times 10^{-12}$ [F/m], permittivity of vacuum

$m_e = 9.1 \times 10^{-31}$ [kg]

$e = 1.6 \times 10^{-19}$ [C], electron charge

$\hbar = 6.58 \times 10^{-16}$ [eV · s/rad], reduced Planck constant

$E_h = m_e e^4/\hbar^2 = 2Ry = 27.2114$ [eV], Hartree energy

$Ry = 13.6$ [eV], Rydberg energy

$a_0 = \hbar^2/(m_e e^2) = 5.29177 \times 10^{-9}$ [cm], Bohr radius

$\pi e^4 = \pi(a_0 E_h)^2 = 6.5141 \times 10^{-14}$ [cm^2 eV^2]

$m_e c^2 = 510.999$ [keV], rest energy of the electron

The Fermi energy can be estimated using the number of electrons per unit volume as

$$E_F = 3.64645 \times 10^{-15} n^{2/3}\ [\text{eV}] = 1.69253 \text{n}_0^{2/3} [\text{eV}]$$

where n and n_0 are in the units of [cm^{-3}] and $n = n_0 \times 10^{22}$. The Fermi wave number is calculated as

$$k_F = 6.66511 \times 10^7 n_0^{1/3}\ [\text{cm}^{-1}].$$

The Fermi velocity is calculated as

$$v_F = 7.71603 \times 10^7 n_0^{1/3} [\text{cm/s}].$$

Appendix C. Program flowchart

Fig. 7.

Appendix D. Definition of coordinate system

The basic geometry for the simulation assumes that the electron undergoes an elastic scattering event at some point P_n, having traveled to P_n from a previous scattering event at $P_{\text{n}-1}$ as shown in Fig. 8. To calculate the position of the new scattering point $P_{\text{n}+1}$, we first require to know the distance Δs_{n+1} between $P_{\text{n}+1}$ and the preceding point P_n.

The path is described using direction cosines, ca, cb and cc. The coordinates at the end of the step at $P_{\text{n}+1}, x_{\text{n}+1}, y_{\text{n}+1}$ and $z_{\text{n}+1}$, are then related to the coordinates x_n, y_n and z_n at P_n by the formulas [65]

$$x_{n+1} = x_n + \Delta s_{n+1} \cdot ca$$
$$y_{n+1} = y_n + \Delta s_{n+1} \cdot cb$$
$$z_{n+1} = z_n + \Delta s_{n+1} \cdot cc$$

The direction cosines ca, cb, cc are found from the direction cosines cx, cy and cz with which the electron reached P_n. The result is

$$ca = (cx \cdot \cos\theta) + (V1 \cdot V3) + (cy \cdot V2 \cdot V4)$$
$$cb = (cy \cdot \cos\theta) + (V4 \cdot (cz \cdot V1 - cx \cdot V2))$$
$$cc = (cz \cdot \cos\theta) + (V2 \cdot V3) - (cy \cdot V1 \cdot V4)$$

where

$$V1 = AN \cdot \sin\theta$$
$$V2 = AM \cdot AN \sin\theta$$
$$V3 = \cos\phi$$
$$V4 = \sin\phi$$

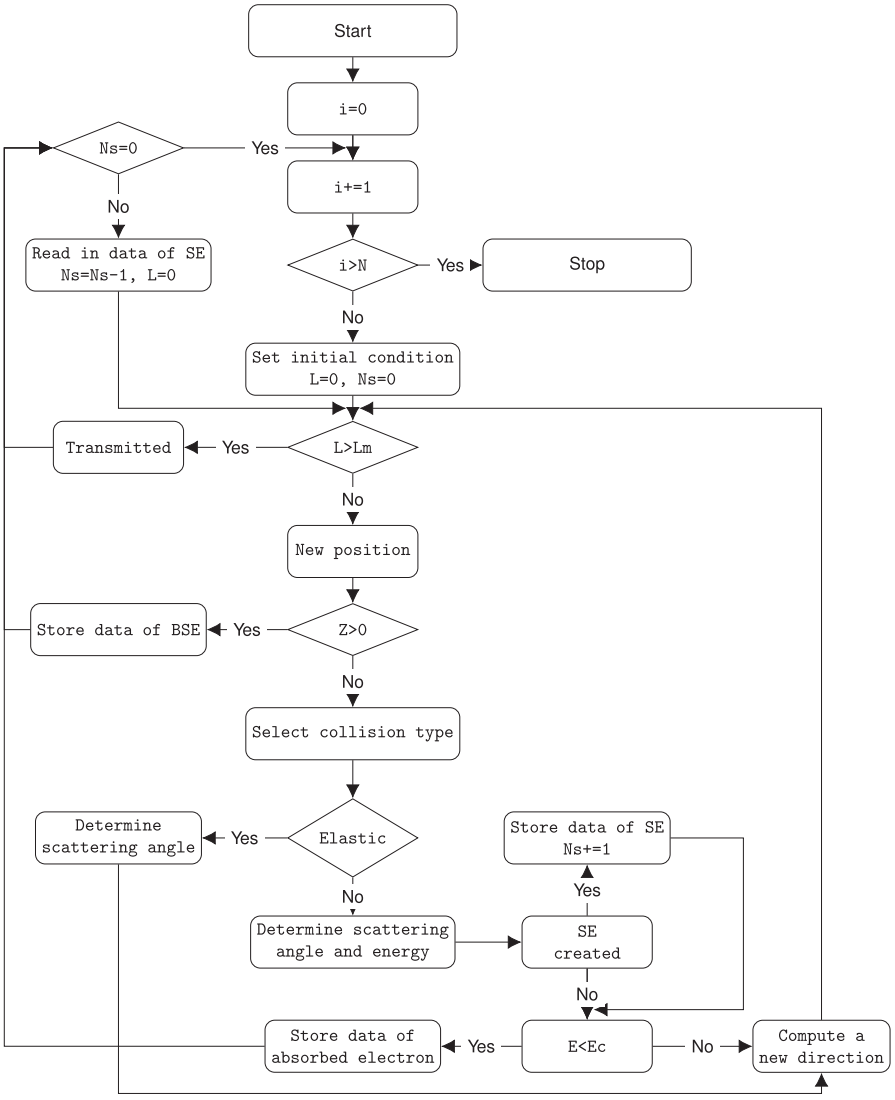

Fig. 7. Flow chart of the Monte Carlo program.

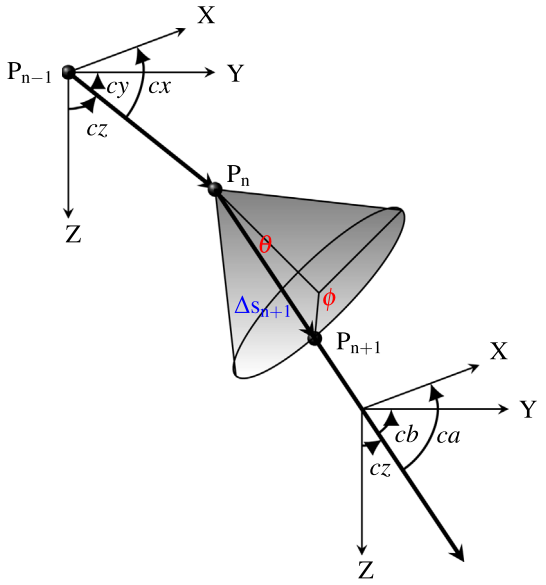

Fig. 8. Definition of coordinate system used in the Monte Carlo simulation program.

and

$$AM = -\frac{cx}{cz}$$

$$AN = \frac{1}{\sqrt{1 + AM \cdot AM}}$$

References

[1] G. Hobbs, J. Wesson, Heat flow through a Langmuir sheath in the presence of electron emission, Plasma Phys. 9 (1) (1967) 85.
[2] Y. Raitses, D. Staack, M. Keidar, N. Fisch, Electron-wall interaction in hall thrusters a, Phys. Plasmas 12 (5) (2005) 057104.
[3] Y. Raitses, A. Smirnov, D. Staack, N. Fisch, Measurements of secondary electron emission effects in the hall thruster discharge, Phys. Plasmas 13 (1) (2006) 014502.
[4] D.M. Goebel, I. Katz, Fundamentals of Electric Propulsion: Ion and Hall Thrusters, vol. 1, John Wiley & Sons, 2008.
[5] S. Mazouffre, Electric propulsion for satellites and spacecraft: established technologies and novel approaches, Plasma Sources Sci. Technol. 25 (3) (2016) 033002.
[6] H. Wiedemann, Particle Accelerator Physics, Springer, 2015.
[7] G. McCracken, P. Stott, Plasma-surface interactions in tokamaks, Nucl. Fusion 19 (7) (1979) 889.
[8] I. Kaganovich, Y. Raitses, D. Sydorenko, A. Smolyakov, Kinetic effects in a hall thruster discharge a, Phys. Plasmas 14 (5) (2007) 057104.

[9] J. Gunn, Evidence for strong secondary electron emission in the tokamak scrape-off layer, Plasma Phys. Control. Fusion 54 (8) (2012) 085007.
[10] W. Lee, S.I. Krasheninnikov, Secondary electron emission and the bifurcation of the heat flux to the targets in fusion plasmas, Phys. Plasmas 20 (12) (2013) 122501.
[11] D.E. Post, R. Behrisch, Physics of Plasma-Wall Interactions in Controlled Fusion, Springer Science & Business Media, 2013.
[12] H. Seiler, Secondary electron emission in the scanning electron microscope, J. Appl. Phys. 54 (11) (1983) R1–R18.
[13] L. Reimer, Scanning electron microscopy: physics of image formation and microanalysis, 2000.
[14] K.-J. Kim, Rf and space-charge effects in laser-driven rf electron guns, Nucl. Instrum. Methods Phys. Res., Sect. A 275 (2) (1989) 201–218.
[15] P. Chabert, N. Braithwaite, Physics of Radio-Frequency Plasmas, Cambridge University Press, 2011.
[16] C. Charles, R. Boswell, K. Takahashi, Investigation of radiofrequency plasma sources for space travel, Plasma Phys. Control. Fusion 54 (12) (2012) 124021.
[17] A. Dunaevsky, Y. Raitses, N. Fisch, Secondary electron emission from dielectric materials of a hall thruster with segmented electrodes, Phys. Plasmas 10 (6) (2003) 2574–2577.
[18] D. Sydorenko, I. Kaganovich, Y. Raitses, A. Smolyakov, Breakdown of a space charge limited regime of a sheath in a weakly collisional plasma bounded by walls with secondary electron emission, Phys. Rev. Lett. 103 (14) (2009) 145004.
[19] M. Campanell, A. Khrabrov, I. Kaganovich, Instability, collapse, and oscillation of sheaths caused by secondary electron emission, Phys. Plasmas 19 (12) (2012) 123513.
[20] J. Sheehan, I. Kaganovich, H. Wang, D. Sydorenko, Y. Raitses, N. Hershkowitz, Effects of emitted electron temperature on the plasma sheath, Phys. Plasmas 21 (6) (2014) 063502.
[21] S. Langendorf, M. Walker, Effect of secondary electron emission on the plasma sheath, Phys. Plasmas 22 (3) (2015) 033515.
[22] L. Wang, T. Raubenheimer, G. Stupakov, Suppression of secondary emission in a magnetic field using triangular and rectangular surfaces, Nucl. Instrum. Methods Phys. Res., Sect. A 571 (3) (2007) 588–598.
[23] M. Pivi, F. King, R. Kirby, T. Raubenheimer, G. Stupakov, F. Le Pimpec, Sharp reduction of the secondary electron emission yield from grooved surfaces, J. Appl. Phys. 104 (10) (2008) 104904.
[24] V. Nistor, L.A. González, L. Aguilera, I. Montero, L. Galán, U. Wochner, D. Raboso, Multipactor suppression by micro-structured gold/silver coatings for space applications, Appl. Surf. Sci. 315 (2014) 445–453.
[25] J.M. Sattler, R.A. Coutu, R.A. Lake, T. Laurvick, Engineered surfaces to control secondary electron emission for multipactor suppression, in: 2016 IEEE National Aerospace and Electronics Conference (NAECON) and Ohio Innovation Summit (OIS), IEEE, 2016, pp. 296–302.
[26] V. Baglin, J. Bojko, C. Scheuerlein, O. Gröbner, M. Taborelli, B. Henrist, N. Hilleret, The secondary electron yield of technical materials and its variation with surface treatments, Tech. rep., 2000.
[27] Y. Suetsugu, H. Fukuma, K. Shibata, M. Pivi, L. Wang, et al., Experimental studies on grooved surfaces to suppress secondary electron emission, in: Proc. IPAC10, paper TUPD043.
[28] L. Aguilera, I. Montero, M. Dávila, A. Ruiz, L. Galán, V. Nistor, D. Raboso, J. Palomares, F. Soria, Cuo nanowires for inhibiting secondary electron emission, J. Phys. D: Appl. Phys. 46 (16) (2013) 165104.
[29] Y. Raitses, I. Kaganovich, A. Sumant, Electron emission from nano-and micro-engineered materials relevant to electric propulsion, in: Proceedings of the 33rd International Electric Propulsion Conference, Washington DC, USA, 2013.
[30] M. Patino, Y. Raitses, R. Wirz, Secondary electron emission from plasma-generated nanostructured tungsten fuzz, Appl. Phys. Lett. 109 (20) (2016) 201602.
[31] D. Staack, Y. Raitses, N. Fisch, Shielded electrostatic probe for nonperturbing plasma measurements in hall thrusters, Rev. Sci. Instrum. 75 (2) (2004) 393–399.
[32] J. Sheehan, Y. Raitses, N. Hershkowitz, I. Kaganovich, N. Fisch, A comparison of emissive probe techniques for electric potential measurements in a complex plasma, Phys. Plasmas 18 (7) (2011) 073501.
[33] J. Sheehan, Y. Raitses, N. Hershkowitz, M. McDonald, Recommended practice for use of emissive probes in electric propulsion testing, J. Propul. Power.
[34] N.F. Mott, The scattering of fast electrons by atomic nuclei, Proc. Roy. Soc. Lond.. Ser. A, Contain. Papers Math. Phys. Charact. 124 (794) (1929) 425–442.
[35] D.C. Joy, Monte Carlo Modeling for Electron Microscopy and Microanalysis, vol. 9, Oxford University Press, 1995.
[36] L. Reimer, R. Senkel, Monte carlo simulations in low voltage scanning electron microscopy, Optik 98 (3) (1995) 85–94.
[37] Z. Czyżewski, D.O. MacCallum, A. Romig, D.C. Joy, Calculations of mott scattering cross section, J. Appl. Phys. 68 (7) (1990) 3066–3072.
[38] R. Browning, T. Li, B. Chui, J. Ye, R. Pease, Z. Czyżewski, D. Joy, Empirical forms for the electron/atom elastic scattering cross sections from 0.1 to 30 kev, J. Appl. Phys. 76 (4) (1994) 2016–2022.
[39] R. Browning, T. Li, B. Chui, J. Ye, R. Pease, Z. Czyzewski, D. Joy, Low-energy electron/atom elastic scattering cross sections from 0.1 to 30 kev, Scanning 17 (4) (1995) 250–253.
[40] D. Drouin, R. Gauvin, D.C. Joy, Computation of polar angle of collisions from partial elastic mott cross-sections, Scanning 16 (2) (1994) 67–77.
[41] R.F. Egerton, Electron Energy-Loss Spectroscopy in the Electron Microscope, Springer Science & Business Media, 2011.
[42] Y. Lin, A study of the secondary electrons.
[43] H. Bethe, Zur theorie des durchgangs schneller korpuskularstrahlen durch materie, Ann. Phys. 397 (3) (1930) 325–400.
[44] M. Dapor, Transport of energetic electrons in solids, Springer Tracts Mod. Phys. 257 (2014) 81.
[45] D. Joy, S. Luo, An empirical stopping power relationship for low-energy electrons, Scanning 11 (4) (1989) 176–180.
[46] J. Fernández-Varea, R. Mayol, D. Liljequist, F. Salvat, Inelastic scattering of electrons in solids from a generalized oscillator strength model using optical and photoelectric data, J. Phys.: Condens. Matter 5 (22) (1993) 3593.
[47] A. Jablonski, S. Tanuma, C.J. Powell, New universal expression for the electron stopping power for energies between 200 eV and 30 keV, Surf. Interface Anal. 38 (2) (2006) 76–83.
[48] A. Taborda, A. Desbrée, M. Reis, Simple polynomial approximation to modified bethe formula low-energy electron stopping powers data, Nucl. Instrum. Methods Phys. Res., Sect. B 356 (2015) 172–175.
[49] A. Jablonski, S. Tanuma, C.J. Powell, A predictive formula for the electron stopping power, Surf. Interface Anal.
[50] D.C. Joy, A database on electron-solid interactions, Scanning 17 (5) (1995) 270–275.
[51] R. Shimizu, Y. Kataoka, T. Ikuta, T. Koshikawa, H. Hashimoto, A monte carlo approach to the direct simulation of electron penetration in solids, J. Phys. D: Appl. Phys. 9 (1) (1976) 101.
[52] I. Adesida, R. Shimizu, T. Everhart, A study of electron penetration in solids using a direct monte carlo approach, J. Appl. Phys. 51 (11) (1980) 5962–5969.
[53] R. Shimizu, D. Ze-Jun, Monte carlo modelling of electron-solid interactions, Rep. Prog. Phys. 55 (4) (1992) 487.
[54] Z.-J. Ding, R. Shimizu, A monte carlo modeling of electron interaction with solids including cascade secondary electron production, Scanning 18 (2) (1996) 92–113.
[55] H.-J. Fitting, Transmission, energy distribution, and se excitation of fast electrons in thin solid films, Phys. Stat. Solidi (a) 26 (2) (1974) 525–535.
[56] M. Gryziński, Classical theory of electronic and ionic inelastic collisions, Phys. Rev. 115 (2) (1959) 374.
[57] M. Gryziński, Classical theory of atomic collisions. I. Theory of inelastic collisions, Phys. Rev. 138 (2A) (1965) A336.
[58] M. Gryziński, Two-particle collisions. I. General relations for collisions in the laboratory system, Phys. Rev. 138 (2A) (1965) A305.
[59] M. Gryziński, Two-particle collisions. II. Coulomb collisions in the laboratory system of coordinates, Phys. Rev. 138 (2A) (1965) A322.
[60] A. Bentabet, N. Bouarissa, Electrons impinging on solid targets: an approximation of the differential elastic scattering cross-section, Phys. Lett. A 355 (4) (2006) 390–393.
[61] H. Stolz, Zur theorie der sekundärelektronenemission von metallen der transportprozeß, Ann. Phys. 458 (3–4) (1959) 197–210.
[62] R.A. Ferrell, Angular dependence of the characteristic energy loss of electrons passing through metal foils, Phys. Rev. 101 (2) (1956) 554.
[63] R.A. Ferrell, Characteristic energy loss of electrons passing through metal foils. ii. dispersion relation and short wavelength cutoff for plasma oscillations, Phys. Rev. 107 (2) (1957) 450.
[64] D.C. Joy, A.D. Romig Jr., J. Goldstein, Principles of Analytical Electron Microscopy, Springer Science & Business Media, 1986.
[65] K.F. Heinrich, D.E. Newbury, H. Yakowitz, Use of Monte Carlo calculations in electron probe microanalysis and scanning electron microscopy: proceedings of a workshop held at the National Bureau of Standards, Gaithersburg, Maryland, October 1-3, 1975, no. 460, US Dept. of Commerce, National Bureau of Standards: for sale by the Supt. of Docs., US Govt. Print. Off., 1976.
[66] A.J. Ahearn, The emission of secondary electrons from tungsten, Phys. Rev. 38 (10) (1931) 1858.
[67] E.A. Coomes, Total secondary electron emission from tungsten and thorium-coated tungsten, Phys. Rev. 55 (6) (1939) 519.
[68] I. Bronshtein, B. Fraiman, Honchnaya electronnaya emissia, (secondary electron emission, in Russian), 1969.
[69] Z. Ding, X. Tang, R. Shimizu, Monte carlo study of secondary electron emission, J. Appl. Phys. 89 (1) (2001) 718–726.
[70] C. Walker, M. El-Gomati, A. Assa'd, M. Zadražil, The secondary electron emission yield for 24 solid elements excited by primary electrons in the range 250–5000 eV: a theory/experiment comparison, Scanning 30 (5) (2008) 365–380.
[71] J. Marian, L.A. Zepeda-Ruiz, N. Couto, E.M. Bringa, G.H. Gilmer, P.C. Stangeby, T. D. Rognlien, Characterization of sputtering products during graphite exposure to deuterium ions by molecular dynamics, J. Appl. Phys. 101 (4) (2007) 044506.
[72] M. Schmidt, H. Lipson, Distilling free-form natural laws from experimental data, science 324 (5923) (2009) 81–85.
[73] M. Schmidt, H. Lipson, Eureqa (version 0.98 beta)[software], Nutonian, Somerville, Mass, USA.
[74] D.R. Penn, Electron mean-free-path calculations using a model dielectric function, Phys. Rev. B 35 (2) (1987) 482.
[75] T. Koshikawa, R. Shimizu, A monte carlo calculation of low-energy secondary electron emission from metals, J. Phys. D: Appl. Phys. 7 (9) (1974) 1303.
[76] M. Kotera, A monte carlo simulation of primary and secondary electron trajectories in a specimen, J. Appl. Phys. 65 (10) (1989) 3991–3998.